Vacuum 206 (2022) 111528

Contents lists available at ScienceDirect

Vacuum

journal homepage: www.elsevier.com/locate/vacuum

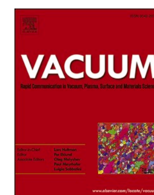

Study on CoAl intermetallic compound films for advanced interconnect applications: Experimental and DFT investigations

Kyeong-Youn Song [a,1], Jin Soo Lee [b,1], Youngjun Lee [b], Minwoo Cho [c], Hoon Choi [d], Young-Kyun Kwon [b,e,*], Hoo-Jeong Lee [a,c,d,**]

[a] SKKU Advanced Institute of Nano Technology, Sungkyunkwan University, Suwon, 16419, Republic of Korea
[b] Department of Physics, Kyung Hee University, Seoul, 02447, Republic of Korea
[c] School of Advanced Materials Science and Engineering, Sungkyunkwan University, Suwon, 16419, Republic of Korea
[d] Department of Smart Fab. Technology, Sungkyunkwan University, Suwon, 16419, Republic of Korea
[e] Department of Information Display and Research Institute for Basic Sciences, Kyung Hee University, Seoul, 02447, Republic of Korea

ARTICLE INFO

Keywords:
CoAl
Interconnect
DFT
Electrical resistivity
Metallization
Microstructure

ABSTRACT

This paper reports the results of a materials study on co-sputtered CoAl thin films for interconnect applications based on both experiments and computations. We modulate the composition and microstructure of the CoAl films by controlling the deposition conditions (sputtering power, substrate temperature, and deposition time). The morphology and microstructure of the films are investigated using scanning electron microscopy, X-ray diffraction, and transmission electron microscopy. The measurement of the film resistivity reveals a strong stoichiometry effect: the lowest (~30 μΩ•cm) for the stoichiometric film. It also discloses a typical trend of size dependence: the resistivity increases rapidly with the thickness decreasing (from 38 μΩ•cm for 43 nm to 72 μΩ•cm for 13 nm). We also compute the resistivity dependence on the film thickness by solving the Boltzmann transport equation with inputs of the electronic and phononic structures from the first-principles density functional theory and the electron-phonon relaxation time modified according to the film thickness. Furthermore, we devised a simple model considering the effects of grain sizes and scattering at grain boundaries on the resistivity to describe the transport behavior in CoAl. Our calculated results were found consistent with our experimentally observed ones.

1. Introduction

Copper (Cu) has been vastly used as an interconnect material for a long time because of its low bulk resistivity and good device reliability, such as electromigration (EM) and time-dependent dielectric breakdown (TDDB) [1,2]. It has been, however, reported that in a narrow Cu metal line adopted in recent technology nodes (beyond 32 nm metal pitch), its electrical resistivity increases sharply due to electron scattering at the surface as well as grain boundaries, while EM and TDDB failure times decreases [3–9]. To overcome such an obstacle for Cu, there have been lots of studies exploring new interconnect materials with the combination of a high conductivity at a narrow linewidth and good reliability. Among them, several theoretical analyses commonly suggested two criteria as a guideline: a low $\rho_0 \times \lambda$ (ρ_0: bulk resistivity, λ:electron mean free path) value and high cohesive energy [5,10–13]. In this regard, Co and Ru have been actively studied as Cu replacement or liner materials and have been applied to recent logic devices [14–18]. Nevertheless, it is expected that as scaling-down continues, extra resistance arising from liner and/or barrier, still required for Co and Ru metallization, could be increasingly burdensome. Thus, urgent is search for a new interconnect material with a challenging combination of stability high enough to ensure reliability without liner/barrier and high conductivity.

Recently, binary compounds (aluminides, silicides, and germanides) have attracted much attention due to their relatively low resistivity and strong chemical bonding [19–24]. It was, for example, shown that aluminides (such as $CuAl_2$, NiAl, Al_3Sc, etc) have the potential as a low-resistivity material [19,25–28]. A study done by Chen et al. on $CuAl_2$ showed its excellent electrical properties and good wettability

* Corresponding author. Department of Physics, Kyung Hee University, Seoul, 02447, Republic of Korea.
** Corresponding author. Department of Smart Fab. Technology, Sungkyunkwan University, Suwon, 16419, Republic of Korea.
E-mail addresses: ykkwon@khu.ac.kr (Y.-K. Kwon), hlee@skku.edu (H.-J. Lee).
[1] These 1st authors equally contributed to this work.

https://doi.org/10.1016/j.vacuum.2022.111528
Received 8 August 2022; Received in revised form 19 September 2022; Accepted 20 September 2022
Available online 24 September 2022
0042-207X/© 2022 Elsevier Ltd. All rights reserved.

[19]. However, $CuAl_2$ has several problems such as diffusion of Al atoms into the dielectrics, which would increase the parasitic capacitance and lead to a rapid increase in resistivity at a very thin thickness (<10 nm) [19,29]. CoAl is another promising aluminide for Cu replacement owing to its high electrical and thermal conductivities, oxidation resistance, and high stability [30–33]. Nevertheless, what remains unexplored is a systematic analysis of the microstructure and electrical properties of CoAl thin films.

Here we embarked on a thorough materials study of co-sputtered CoAl thin films for interconnect applications. We fabricated CoAl films of different compositions under various deposition conditions (substrate temperatures and deposition time). Careful materials analysis using scanning electron microscopy, X-ray diffraction, and transmission electron microscopy allowed us to investigate the morphology and microstructure of the films. We measured the resistivity of the films to understand the effects of the film thickness, substrate temperature, and film composition. We also performed first-principle calculations to investigate the structural, electronic, and phonon properties of Co–Al alloy, with which one can evaluate the energy-momentum dependent relaxation time. We also estimated the film thickness-dependent mean free path and thus relaxation time, which allowed us to elucidate the size-dependent resistivity of Co–Al films measured in our experiment.

2. Methodology

2.1. Experimentation

The CoAl films were deposited on a Si (100) wafer covered with 100 nm of thermally grown SiO_2 using magnetron co-sputtering by pure Co and Al targets. The base pressure of the sputtering chamber was $\sim 1.3 \times 10^{-5}$ Pa and the working pressure was 0.72 Pa in an Ar ambient. Films were deposited at various substrate temperatures between room temperature and 500 °C. The base pressure with different substrate temperatures was measured around 4.0×10^{-4} Pa at 300 °C, and 2.7×10^{-3} Pa at 500 °C. To control the composition, the target power for the Co target was modulated, while that for Al was kept constant. For characterization of the phases of the films, grazing incidence X-Ray diffraction (GIXRD, Rigaku Smart lab) with an incidence angle of 0.5° was utilized. The film surface and thickness were analyzed employing field-emission scanning electron microscopy (FESEM, Hitachi, SU8220). For films of less than 30 nm, the thickness was measured using X-ray reflectivity (XRR, Rigaku Smart lab). Transmission electron microscopy (TEM, JEOL JEM-2100F, operating at 200 kV) and energy-dispersive X-ray spectroscopy (EDS) was used for the investigation of microstructure and chemical composition. Electron probe microanalysis (EPMA, Shimadzu EPMA-1600) was used to determine the film composition, cross-checked with inductively coupled plasma–optical emission spectrometry (ICP-OES, Thermo fisher scientific iCAP 6000 SERIES). Sheet resistance (R_s) was measured by a 4-point probe (CMT-SR2000 N) and the resistivity was calculated by multiplying R_s and film thickness.

2.2. Computation

To investigate the electrical transport property of CoAl, we first carried out first-principles calculations based on the density functional theory [34] as implemented in Quantum Espresso code [35] to calculate the electronic structures. The electronic wavefunctions were expanded in terms of plane wave basis with a kinetic energy cutoff of 80 Ry for CoAl and 240 Ry for Cu and Ru. We used the scalar relativistic norm-conserving pseudopotentials [36,37] to describe the core and valence electrons and treated the exchange-correlation functional within the local density approximation of Perdew-Wang [38] obtained from the pseudo-dojo [39]. The Brillouin zone (BZ) was sampled using a $20 \times 20 \times 20$ Monkhorst-Pack k-points mesh for the integration over the BZ. Then, the phonon calculation was performed using the density functional perturbation theory (DFPT) [40] with a $4 \times 4 \times 4$ q-points grid.

Then, the energy- and temperature-dependent relaxation time $\tau(E_{n,\mathbf{k}},T)$ defined as [41,42]

$$\frac{1}{\tau(E_{n,\mathbf{k}},T)} = 2\pi \sum_{m,\nu} \int \frac{d\mathbf{q}}{\Omega_{\mathrm{BZ}}} |\mathscr{G}_{mn,\nu}(\mathbf{k},\mathbf{q})|^2 \{ [f(E_{m,\mathbf{k}+\mathbf{q}},T) + g(\omega_{\nu,\mathbf{q}},T)] \delta(E_{n,\mathbf{k}} - E_{m,\mathbf{k}+\mathbf{q}} + \omega_{\nu,\mathbf{q}}) + [1 - f(E_{m,\mathbf{k}+\mathbf{q}},T) + g(\omega_{\nu,\mathbf{q}},T)] \delta(E_{n,\mathbf{k}} - E_{m,\mathbf{k}+\mathbf{q}} - \omega_{\nu,\mathbf{q}}) \}$$

was evaluated for given n and $\mathbf{k}$. Note that this equation represents solely the electron-phonon relaxation time since it mainly contributes to conductors at room temperature. Note that this equation is expressed in atomic units ($\hbar = e = 1$). Here $\sum_{m,\nu}$ and $\int \frac{d\mathbf{q}}{\Omega_{\mathrm{BZ}}}$ denote the summation over both electronic band and phonon branch indices m and ν, and the normalized $\mathbf{q}$-space integration over the whole BZ with its volume Ω_{BZ}, respectively. To represent the electronic and phononic occupations for their corresponding energy eigenvalues $E_{m,\mathbf{k}+\mathbf{q}}$ and $\omega_{\nu,\mathbf{q}}$ at temperature T, the Fermi-Dirac and Bose-Einstein distributions, $f(E_{m,\mathbf{k}+\mathbf{q}},T)$ and $g(\omega_{\nu,\mathbf{q}},T)$ were used. $\delta(\varepsilon)$ is the usual Dirac delta function. $\mathscr{G}_{mn,\nu}(\mathbf{k},\mathbf{q})$ is the first-order electron-phonon matrix element given by $m,\mathbf{k}+\mathbf{q}|\partial_{\nu,\mathbf{q}}V|n,\mathbf{k}/\sqrt{2\omega_{\nu,\mathbf{q}}}$ with $\partial_{\nu,\mathbf{q}}V$ the derivative of the self-consistent potential associated with a phonon mode $\omega_{\nu,\mathbf{q}}$. [42,45] It is related to the probability amplitude of the phonon-mediated scattering process from a state $|n,\mathbf{k}$ to another $|m,\mathbf{k}+\mathbf{q}$. $\mathscr{G}_{mn,\nu}(\mathbf{k},\mathbf{q})$ was computed by employing DFPT on the same k- and q-points meshes and then using maximally localized Wannier functions [43–45] through the EPW package [41,46]

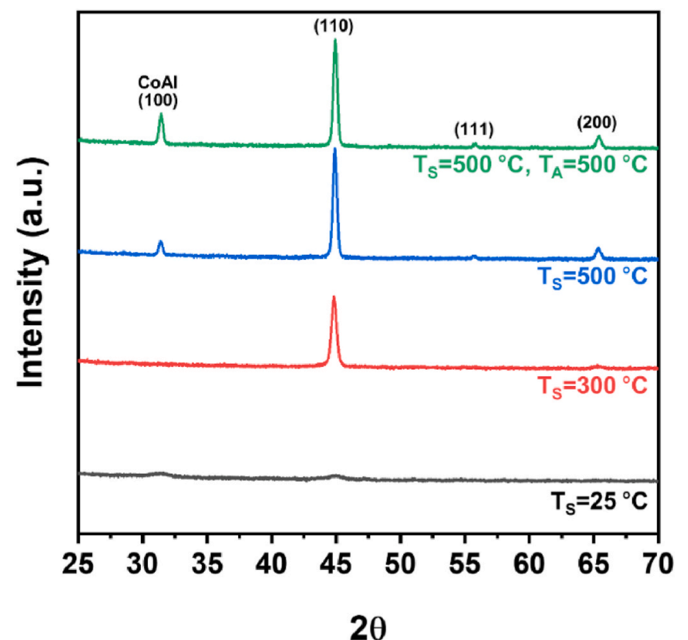

Fig. 1. GIXRD results of CoAl thin films at the different substrates (T_S) and post-annealing (T_A) temperatures.

to interpolate over 60 × 60 × 60 fine *k*-points and randomly-sampled 10,000 fine *q*-points grids. This relaxation time was used to solve the Boltzmann transport equation, which allows us to evaluate the electrical conductivity [47].

3. Results and discussion

3.1. Structural and morphological analysis

Fig. 1 shows GIXRD spectra of CoAl thin films of composition close to the stoichiometric composition, grown at various deposition temperatures (T_S) from room temperature to 500 °C. The deposition time was kept constant at 20 min, and additional post-annealing (T_A) at 500 °C was also done for the 500°C-deposited film. For the as-deposited film, broad and low peaks appear, indicating that the thin film has a small grain size and low crystallinity. The positions of the peaks are found consistent with those of the B2 phase of CoAl among several intermetallic compounds of the Co–Al system (such as Al_5Co_2, CoAl, Al_3Co, $Al_{13}Co_4$, Al_9Co_2, etc) [48,49]. As the deposition temperature rises to 300 °C and 500 °C, the peak intensity of CoAl increases, suggesting a significant increase in crystallinity. For the sample annealed at 500 °C after being deposited at 500 °C, the peaks appear similar to those of the 500°C-deposited sample, without showing other peaks suggestive of a possible reaction such as oxidation.

The surface morphology of the CoAl thin films with different T_S was characterized using SEM, as shown in Fig. 2. The as-deposited film shows a fine granular surface morphology with a high density of nanopores (Fig. 2(a)). The granular features changed to a faceted, triangular shape with a larger size for the 300°C-deposited sample (Fig. 2(b)). Such faceted film growth is possibly due to anisotropy in the growth rate of the different crystal planes of CoAl [50]. The 500 °C sample displays large surface features with almost no gap between them, suggesting that grain growth has occurred and that the film has become dense. It appears that the high substrate temperature (500 °C) probably imparted to the sputtered atoms a surface mobility high enough to prompt grain growth and thus the formation of a dense film [50]. In addition, Fig. 2(d–f) display the distribution of the feature size for the three samples, confirming the possible grain growth.

TEM investigation further reveals the details of the microstructure of the films grown at room temperature and 500 °C. Fig. 3 shows the cross-sectional bright-field TEM images and EDS line scan profiles of the samples. The film grown at room temperature shows a columnar structure with very small grains of only several nanometers, as shown in Fig. 3(a). The image taken at a higher magnification, shown in Fig. 3(b), displays regions of a bright contrast between the columns of grains, suggesting the presence of nano-sized pores. These results are consistent with those of the SEM analysis (Fig. 2(a)). For the sample grown at a high temperature (500 °C), on the other hand, grain growth occurred throughout the film. Fig. 3(d) and (e) show a dense film without any pore. Fig. 3(c) and (f) show the result of the EDS analysis carried out along the dotted lines denoted in the images of Fig. 3(a) and (d). The room-temperature film shows a higher oxygen content compared to that of the 500 °C film. The high oxygen content is likely related to the high density of pores since a high concentration of oxygen molecules tends to segregate to such pores [51–53]. In addition, the TEM images and EDS data confirm that no significant interdiffusion has occurred between CoAl and SiO_2 even at a high temperature.

Next, we varied the composition of samples to investigate the effects of the composition on the microstructure and electrical properties of the films. Fig. 4 presents the GIXRD spectra of Co_xAl_{100-x} (x = 43–55) thin films. The spectra appear nearly the same in that there exist two main peaks arising from CoAl. However, a closer examination of the spectra reveals the presence of small peaks corresponding to the Al_5Co_2 phase for the Al-rich films ($Co_{43}Al_{57}$ and $Co_{44}Al_{56}$), as shown in the magnified view in Fig. 4. In contrast, the stoichiometric film and Co-rich films do not show any Al_5Co_2 peaks but show only CoAl peaks. This result is consistent with the phase diagram of the Co–Al system, in which the region of the CoAl phase shows a large solubility of Co but only a small solubility of Al [32].

3.2. Electrical properties

Fig. 5 shows film resistivities for the films of various compositions, grown at room temperature and 500 °C. For the room-temperature films, a resistivity of about 3000 μΩ•cm was measured from the stoichiometric B2 CoAl film. This abnormal high resistivity appears to be due to the high concentration of oxygen, as observed in the TEM and EDS analyses [54]. The resistivity decreases as the cobalt concentration increases since the film becomes metallic. For the 500°C-deposited sample, while the stoichiometric CoAl film has the lowest resistivity (~30 μΩ•cm), the resistivity increases as the composition deviates from the stoichiometric point, showing a V-shaped trend. The increase of the resistivity in the

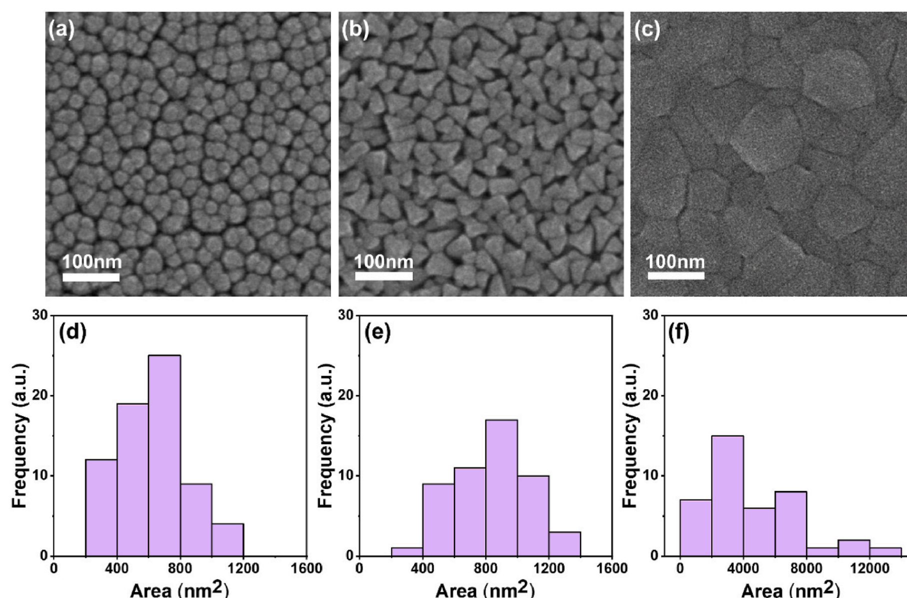

Fig. 2. SEM micrographs of CoAl films deposited at 25 °C (a), 300 °C (b), and 500 °C (c). (d–f) Corresponding features size distributions.

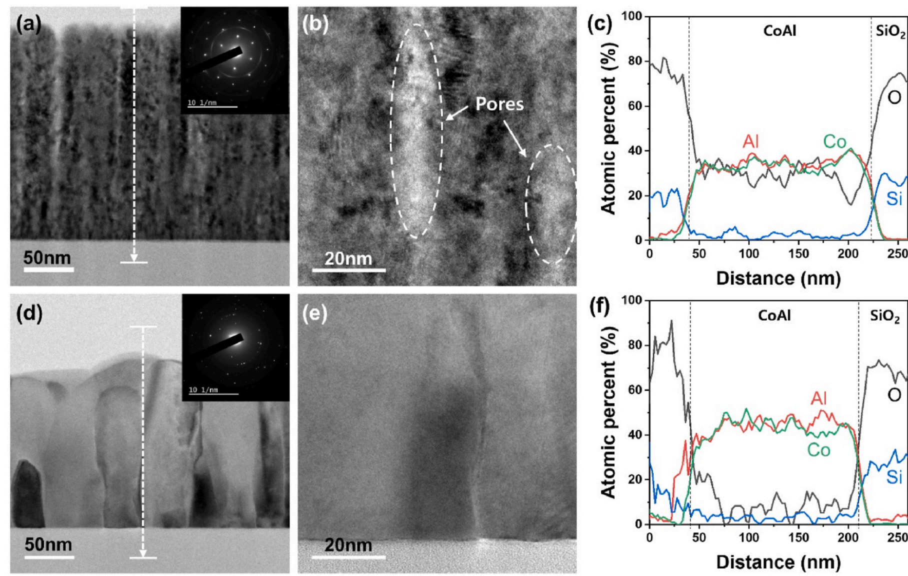

Fig. 3. Cross-sectional TEM images of the CoAl thin films deposited at 25 °C (a,b), and 500 °C (d,e). The inset image in (a) and (d) represents the selected area diffraction pattern (SADP). EDS profile of (c) and (f) was obtained along the white dashed lines denoted in (a) and (d), respectively.

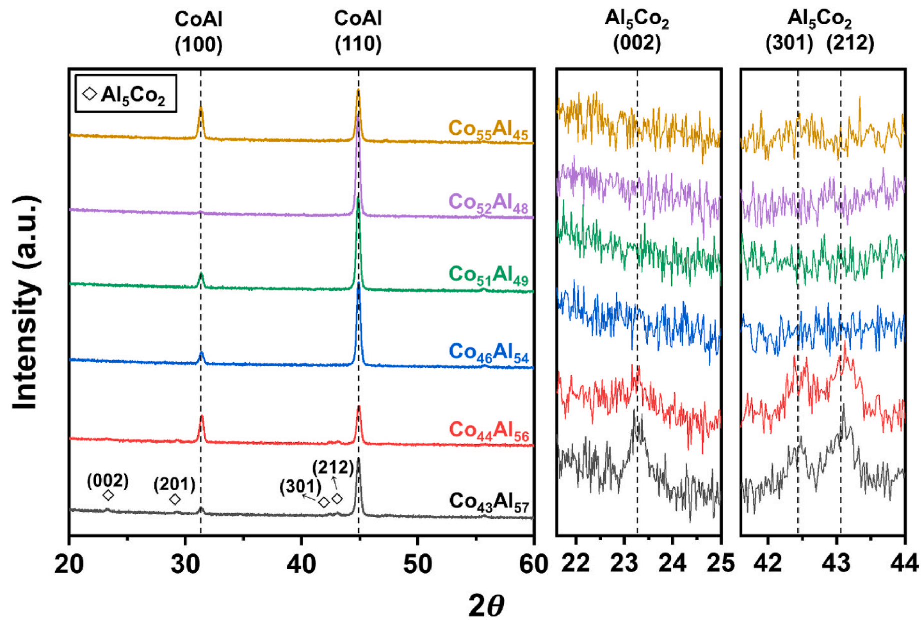

Fig. 4. GIXRD analysis results of CoAl films with different compositions deposited at 500 °C (a magnified view of Al_5Co_2 peaks of (002), (301), and (212) shown right).

off-stoichiometric films could be attributed to a possible presence of a high density of point defects and the formation of such intermetallic compounds as Al_5Co_2, as confirmed in the XRD analysis [55].

To fully understand the electronic transport of CoAl, we next theoretically investigated the electrical transport property of CoAl single crystal by carrying out first-principles calculations using the density functional theory described in Methodology section. With the optimized unit cell obtained through the total energy calculation (shown in Fig. 6 (a)), we computed its electronic and phononic band structures shown in Fig. 6(b) and (c). These electronic and phononic structures provided information enabling us to calculate electron relaxation times related to various scattering mechanisms, such as electron-electron relaxation time ($\tau_{\mathrm{el-el}}$), phonon mediated electron-electron relaxation time ($\tau^{\mathrm{ph}}_{\mathrm{el-el}}$), and electron-phonon relaxation time ($\tau_{\mathrm{el}-ph}$). Since the electron-phonon relaxation has a major influence on conductors at room temperature by fermi liquid theory [56], we only employed $\tau_{\mathrm{el}-ph}$, which was calculated using the equation given in Methodology section, to solve the semi-classical Boltzmann transport equation [47]. $\tau(n,\mathbf{k})$ and the group velocity $\mathbf{v}(n,\mathbf{k}) = \frac{1}{\hbar}\nabla_{\mathbf{k}}E_{n,\mathbf{k}}$ calculated from the electronic structure were used to compute the conductivity tensor $\sigma_{\alpha,\beta}$ with α,β indicating x,y,z, given as

$$\sigma_{\alpha,\beta} = \frac{2e^2}{8\pi^3\hbar}\sum_n \iint_{S_F^n} \frac{v_\alpha(n,\mathbf{k})v_\beta(n,\mathbf{k})\tau(n,\mathbf{k})}{|\mathbf{v}(n,\mathbf{k})|} dS \tag{1}$$

where e and $\hbar$ are the electron charge and the reduced Planck constant and $\iint_{S_F^n} dS$ denotes the surface integration over the Fermi surface. The

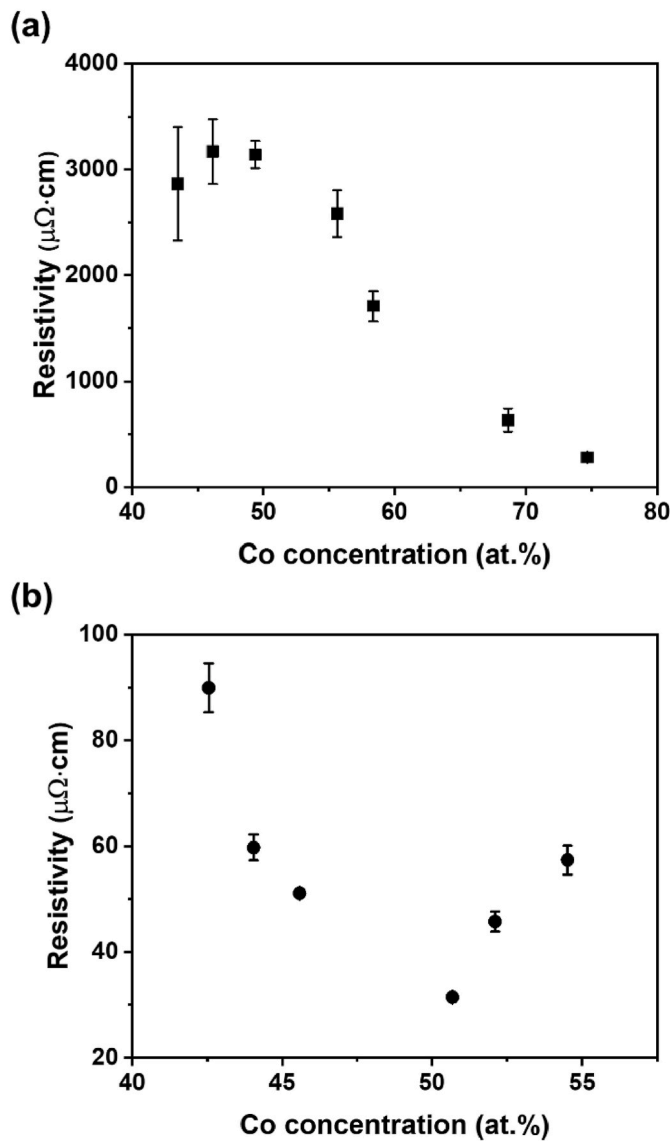

Fig. 5. Resistivity with a Co concentration for CoAl thin films deposited at (a) room temperature, and (b) 500 °C.

conductivity (resistivity) value for the bulk CoAl was calculated to be 2.45×10^7 S/m (4.08 μΩ•cm). We compared the calculated resistivity of CoAl with those of other materials considered as a candidate for interconnect materials, as summarized in Table 1, along with their melting temperatures. It appears that CoAl, with a high melting temperature (1,673 °C, suggestive of high cohesive energy), has a resistivity comparable with other candidates [21].

To include the effects of film thickness and surface direction in addition to transport direction on resistivity, we developed a new method to modify the energy-momentum dependent electron mean free path and thus the relaxation time $\tau_d(n.\mathbf{k})$ for a thin film with a given film thickness d. The electron mean free path λ for each band index n and $\mathbf{k}$ point is evaluated by $\lambda(n, \mathbf{k}) = v(n, \mathbf{k})\tau(n, \mathbf{k})$ with the group velocity $v(n, \mathbf{k})$. For a film with its thickness d, however, $\lambda(n, \mathbf{k})$ will be modified to $\lambda_d(n,\mathbf{k})$, which is smaller than or equal to $\lambda(n,\mathbf{k})$, since if an electron with $n, \mathbf{k}$ moving toward the surface boundary of the film will be scattered out before it travels by $\lambda(n, \mathbf{k})$. Hence, its relaxation time $\tau(n, \mathbf{k})$ can be modified to be $\tau_d(n.\mathbf{k}) = \lambda_d(n, \mathbf{k})/v(n, \mathbf{k})$. Then, the film thickness-dependent conductivity was evaluated using equation (1) with $\tau_d(n.\mathbf{k})$ replacing the bulk relaxation time $\tau(n,\mathbf{k})$. Note that we assumed that the electron scattering at surfaces is diffusive, that is, its specularity for

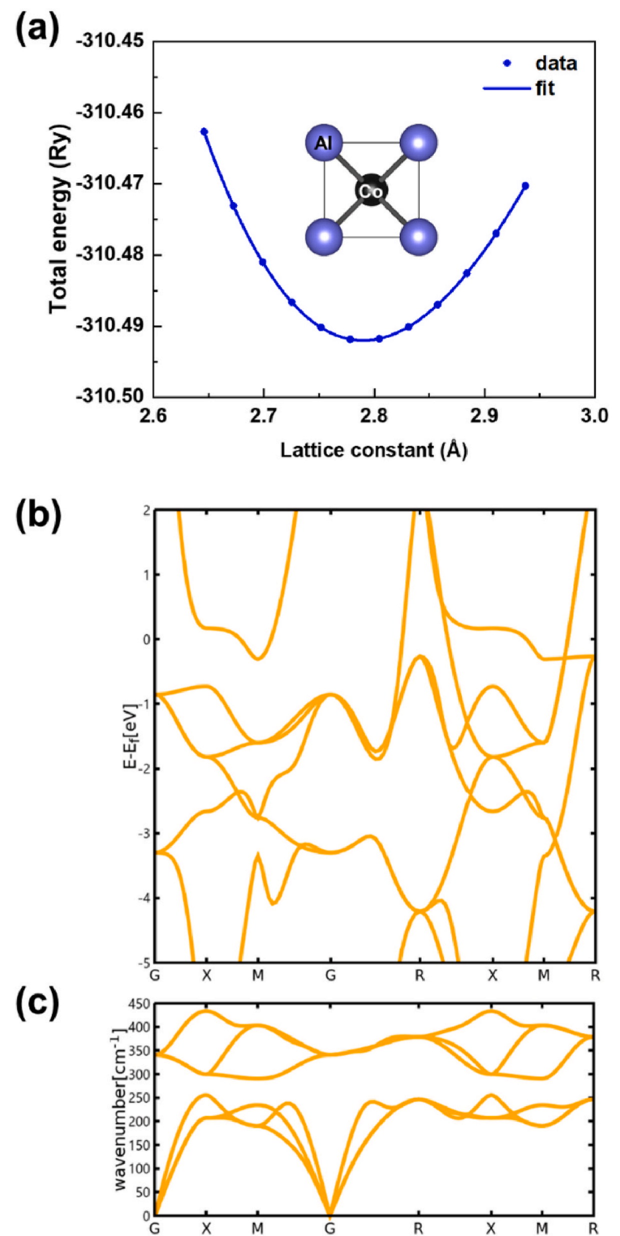

Fig. 6. DFT calculation: (a) total energy as a function of lattice constants, (b) electronic band structure, and (c) phonon dispersion of CoAl single crystal. The inset in (a) shows the unit cell of CoAl.

Table 1
Summary of the reported bulk resistivities and melting points of various metals and alloys.

materials	bulk resistivity (μΩ•cm)		melting point (°C)	references
	experimental	calculated		
CoAl	14.1	[a]4.1	1,673	[32,58]
NiAl	8–10	10.0	1,638	[59,60]
$CuAl_2$	8.0	–	592	[61,62]
Cu	1.7	1.6	1,085	[63]
Co	5.6	[a]8.7	1,495	[60,63,64]
Ru	7.1	[a]6.4	2,334	[63]

[a] The resistivity values of CoAl, Co, and Ru were calculated in this work.

surface scattering to be zero for simplicity [57].

We first calculated the resistivities $\rho(t)$ of CoAl, which are shown as the solid lines in Fig. 7(b), along the same [001] transport direction as a

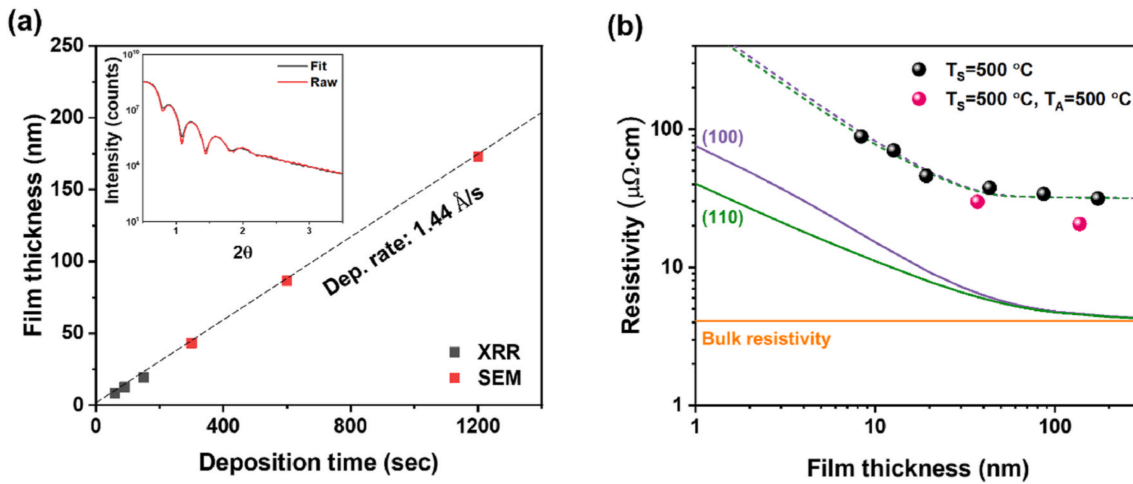

Fig. 7. (a) Film thickness measured by XRR and SEM as a function of deposition time (inset: XRR curve of CoAl film deposited for 150 s), and (b) the resistivity of CoAl as a function of film thickness. In (b), the solid and dashed lines are from the calculation for single crystalline and polycrystalline films, respectively, while the dots (black and pink) are from experiments.

function of film thickness t for (100) and (110) surfaces. It shows that the resistivity of a film increases as the film becomes thinner. An interesting fact is that the resistivity of the film with the (100) surface rises significantly faster than that with the (110) surface, indicating that the resistivity depends not only on the transport direction but also on the out-of-plane direction of the film. Note that these resistivity values were calculated with an ideal CoAl material in a single crystal without any grain boundaries, whereas typical samples contain a high density of grain boundaries. This is why our calculated resistivity values are quite different from our experimental measured values, although they exhibit similar upturn trends as the film becomes thinner, as described below.

We finally measured the resistivity of CoAl of different thicknesses, as shown in Fig. 7. Fig. 7(a) exhibits CoAl film thicknesses, measured by SEM and XRR, with the deposition time. The film thickness is proportional to the deposition time with the slope (the deposition rate) of 1.44 Å/s. Shown in Fig. 7(b) are the measured resistivity data with the film thickness. The graph discloses that the resistivity rises quite rapidly from 38 μΩ•cm at 43 nm to 72 μΩ•cm at 13 nm with the thickness decreasing, as typically observed in interconnect metals. Comparison with the calculated data without grain boundary reveals that the measured data are much higher than the calculated data. The difference could be explained by considering that the calculations were done based on the modeling of defect-free, single-crystalline CoAl and thus the calculated data do not include the effects of scattering with grain boundaries (and other defects) and surface oxide.

To include the effects of grain size and grain boundary scattering on resistivity in our calculations, we devised a simple model in which all grains are assumed to be uniform in size and thus described in terms of a single parameter d_{GB} for grain. In this model, we considered both *intra*- and *inter*-grain resistances. With the film thickness t, the intra-grain resistance for grain with a specific surface i can be calculated by the film-thickness-dependent resistivity $\rho_i(t)$ computed for a single crystalline CoAl film with the specific surface that was already described above, divided by d_{GB}, which is the constant size of grain along the transport direction. On the other hand, the inter-grain resistance can be evaluated by the division of the interfacial resistivity γ_{GB} by the film-thickness-dependent interfacial area $S(t) = d_{GB}d(t)$, where $d(t)$ is the effective grain size for given film thickness t defined by

$$d(t) = \begin{cases} d_{GB} & \text{for } t > d_{GB} \\ d_{GB}\exp\left(\dfrac{t}{d_{GB}} - 1\right) & \text{for } t < d_{GB} \end{cases} \quad (2)$$

The resulting resistivity of the whole film will be given by

$$\rho(t) = \rho_i(t) + \frac{\gamma_{GB}}{d(t)} \quad (3)$$

where the first term is nothing but the average intra-grain resistivity. Note that if the film is in a single crystal ($\gamma_{GB} = 0$) with one type of surface, then $\rho(t) = \rho_i(t)$, which is shown in Fig. 7(b) with the solid lines for $i = (110)$ and $i = (100)$. Equation (3), with Eq. (2), was used to fit our experimentally measured film-thickness dependent resistivity of CoAl film to estimate γ_{GB} and d_{GB}, which were estimated to be 1.40×10^{-7} (1.51×10^{-7}) μΩ•cm^2 and 48 (52) nm, respectively, for the CoAl thin film deposited at $T_S = 500$ °C with the (100) ((110)) surface. $\rho(t)$ of Eq. (3) with these fitted values is shown in Fig. 7(b) with the dashed lines, reflecting our theoretical simple consideration of grain size and grain boundary scattering effects. For the thin film deposited and annealed at $T_S = 500$ °C and $T_A = 500$ °C, those fitted values are 1.63×10^{-7} (1.68×10^{-7}) μΩ•cm^2 and 102 (104) nm, respectively, although there are only two available experimental data. The fitted interfacial values are quite reasonable compared to other cases and the fitted grain size values agree quite well with our experimentally measured values shown in Fig. 2. Note that for single-crystalline thin films, the thickness-dependent resistivity of a film with one specific surface is quite different from that with another specific surface as shown in Fig. 7(b) with solid lines. Such difference becomes less dominant if we consider the effects of grain size and grain boundary scattering, which becomes even more dominant in film resistivity [65].

In this study, we examined the material aspects of CoAl and its electrical properties for interconnect applications. Careful process optimization helped us obtain CoAl films with a resistivity in a range comparable with that of other aluminides. Nevertheless, the data found in our study is somewhat higher than the range of resistivity values reported in other studies on other binary aluminides such as NiAl (about 30 μΩ•cm for 20 nm and 60 μΩ•cm for 10 nm) [20]. Compared with that of a TaN/Cu/TaN film structure (about 9 μΩ•cm for 20 nm and 87 μΩ•cm for 7 nm), a structure close to the current interconnect technology, the resistivity of CoAl seems somewhat higher [66]. However, it should be noted that the extended trend line of the resistivity in Fig. 7 (b), projected by our DFT calculation, indicates that the resistivity increases more slowly than that of Cu, suggesting a possible cross-over for a film thickness below 5 nm.

It should be also noted that there is plenty of room for further improvement of the resistivity for CoAl. This may require an additional process optimization (such as controlling sputtering and post-annealing conditions) to tailor the microstructure, and/or reduce the defect

density and film stress. For example, we introduced an additional post-annealing step (500 °C), which led to a significant reduction in resistivity [~20%, data denoted with the red dots in Fig. 7(b)]. Thus, the results of this study provide data sufficient to confirm the potential of CoAl as a promising candidate for a future interconnect material and warrant further extensive development of the material.

4. Conclusions

In this paper, we reported the results of a thorough materials study on co-sputtered CoAl thin films for interconnect applications. We deposited CoAl films of various compositions by modulating the sputtering power. We also employed various deposition conditions (substrate temperatures and deposition times). Materials characterization using such techniques as scanning electron microscopy, X-ray diffraction, and transmission electron microscopy helped us disclose the morphology and microstructure of the films. The measurement of the film resistivity unraveled that the resistivity dropped sharply as the composition approached the stoichiometry, around 30 μΩ•cm for the stoichiometric film. It also revealed a strong size dependence: the resistivity increases rapidly with the thickness decreasing (from 38 μΩ•cm for 43 nm to 72 μΩ•cm for 13 nm) mainly due to grain boundary scattering, as suggested by our calculations. Comparison with the results of our first principle calculation highlighted that the trend of the resistivity increase appeared quite similar. The results of this study shed some light on the possibility of the material as a future interconnect material through further process optimization.

CRediT authorship contribution statement

Kyeong-Youn Song: Writing – original draft, Methodology, Investigation, Formal analysis, Data curation, Conceptualization. **Jin Soo Lee:** Writing – original draft, Software, Methodology, Investigation, Formal analysis, Data curation. **Youngjun Lee:** Writing – original draft, Software, Methodology, Formal analysis. **Minwoo Cho:** Writing – review & editing, Investigation. **Hoon Choi:** Methodology, Data curation. **Young-Kyun Kwon:** Writing – review & editing, Validation, Supervision, Resources, Project administration, Methodology, Funding acquisition, Formal analysis, Conceptualization. **Hoo-Jeong Lee:** Writing – review & editing, Supervision, Resources, Project administration, Funding acquisition, Conceptualization.

Declaration of competing interest

The authors declare that they have no known competing financial interests or personal relationships that could have appeared to influence the work reported in this paper.

Data availability

The data that has been used is confidential.

Acknowledgments

KYS, MC, HC, and HJL acknowledge financial support from Samsung Electronics Co., Ltd (IO201214-08167-01). JSL, YL, and YKK acknowledge financial support from the Korean government (MSIT) through Institute for Information & Communications Technology Planning & Evaluation (IITP) (2021-0-01580-001) and National Research Foundation (NRF) (NRF-2020R1A5A6017701). Some portion of our computational work was done using the resources of the KISTI Supercomputing Center (KSC-2021-CRE-0479, KSC-2022-CRE-0062).

References

[1] D. Edelstein, J. Heidenreich, R. Goldblatt, W. Cote, C. Uzoh, N. Lustig, P. Roper, T. McDevitt, W. Motsiff, A. Simon, J. Dukovic, R. Wachnik, H. Rathore, R. Schulz, L. Su, Full copper wiring in a sub-0.25 μm CMOS ULSI technology, Tech. Dig. - Int. Electron Devices Meet. IEDM 5 (1997) 773–776, https://doi.org/10.1109/iedm.1997.650496.

[2] C.K. Hu, B. Luther, F.B. Kaufman, J. Hummel, C. Uzoh, D.J. Pearson, Copper interconnection integration and reliability, Thin Solid Films 262 (1995) 84–92, https://doi.org/10.1016/0040-6090(94)05807-5.

[3] H. Kitada, T. Suzuki, T. Kimura, H. Kudo, H. Ochimizu, S. Okano, A. Tsukune, S. Suda, S. Sakai, N. Ohtsuka, T. Tabira, T. Shirasu, M. Sakamoto, A. Matsuura, Y. Asada, T. Nakamura, The influence of the size effect of copper interconnects on RC delay variability beyond 45nm technology, Proc. IEEE 2007 Int. Interconnect Technol. Conf. - Dig. Tech. Pap. (2007) 10–12, https://doi.org/10.1109/iitc.2007.382333.

[4] E.T. Ogawa, K.D. Lee, V.A. Blaschke, P.S. Ho, Electromigration reliability issues in dual-damascene Cu interconnections, IEEE Trans. Reliab. 51 (2002) 403–419, https://doi.org/10.1109/TR.2002.804737.

[5] W. Zhang, S.H. Brongersma, O. Richard, B. Brijs, R. Palmans, L. Froyen, K. Maex, Influence of the electron mean free path on the resistivity of thin metal films, Microelectron. Eng. 76 (2004) 146–152, https://doi.org/10.1016/j.mee.2004.07.041.

[6] A. Pyzyna, R. Bruce, M. Lofaro, H. Tsai, C. Witt, L. Gignac, M. Brink, M. Guillorn, G. Fritz, H. Miyazoe, D. Klaus, E. Joseph, K.P. Rodbell, C. Lavoie, D.G. Park, Resistivity of copper interconnects beyond the 7 nm node, 2015-Augus, Dig. Tech. Pap. - Symp. VLSI Technol. (2015) T120–T121, https://doi.org/10.1109/VLSIT.2015.7223712.

[7] M. Shimada, M. Moriyama, K. Ito, S. Tsukimoto, M. Murakami, Electrical resistivity of polycrystalline Cu interconnects with nano-scale linewidth, J. Vac. Sci. Technol. B Microelectron. Nanom. Struct. 24 (2006) 190, https://doi.org/10.1116/1.2151910.

[8] A.S. Oates, M.H. Lin, The scaling of electromigration lifetimes, IEEE Int. Reliab. Phys. Symp. Proc. (2012) 1–7, https://doi.org/10.1109/IRPS.2012.6241868.

[9] F. Chen, O. Bravo, K. Chanda, P. McLaughlin, T. Sullivan, J. Gill, J. Lloyd, R. Kontra, J. Aitken, A comprehensive study of low-k SiCOH TDDB phenomena and its reliability lifetime model development, IEEE Int. Reliab. Phys. Symp. Proc. (2006) 46–53, https://doi.org/10.1109/RELPHY.2006.251190.

[10] D. Gall, The search for the most conductive metal for narrow interconnect lines, J. Appl. Phys. 127 (2020), https://doi.org/10.1063/1.5133671.

[11] X. Zhang, H. Huang, R. Patlolla, F.W. Mont, X. Lin, M. Raymond, C. Labelle, E. T. Ryan, D. Canaperi, T.E. Standaert, T. Spooner, G. Bonilla, D. Edelstein, Methods to lower the resistivity of ruthenium interconnects at 7 nm node and beyond, IITC 2017 - 2017, IEEE Int. Interconnect Technol. Conf. (2017) 14–16, https://doi.org/10.1109/IITC-AMC.2017.7968941.

[12] S. Dutta, K. Sankaran, K. Moors, G. Pourtois, S. Van Elshocht, J. Bömmels, W. Vandervorst, Z. Tokei, C. Adelmann, Thickness dependence of the resistivity of platinum-group metal thin films, J. Appl. Phys. 122 (2017), https://doi.org/10.1063/1.4992089.

[13] K. Sankaran, S. Clima, M. Mees, C. Adelmann, Z. Tőkei, G. Pourtois, Exploring Alternative Metals to Cu and W for Interconnects : an Ab Initio Insight, 2014, pp. 193–196.

[14] N. Bekiaris, Z. Wu, H. Ren, M. Naik, J.H. Park, M. Lee, T.H. Ha, W. Hou, J.R. Bakke, M. Gage, Y. Wang, J. Tang, Cobalt fill for advanced interconnects, IITC 2017 - 2017, IEEE Int. Interconnect Technol. Conf. (2017) 6–8, https://doi.org/10.1109/IITC-AMC.2017.7968981.

[15] F.W. Mont, X. Zhang, W. Wang, J.J. Kelly, T.E. Standaert, R. Quon, E.T. Ryan, Cobalt interconnect on same copper barrier process integration at the 7nm node, IITC 2017 - 2017, IEEE Int. Interconnect Technol. Conf. (2017) 7–9, https://doi.org/10.1109/IITC-AMC.2017.7968971.

[16] X. Zhang, H. Huang, R. Patlolla, W. Wang, F.W. Mont, J. Li, C.K. Hu, E.G. Liniger, P.S. McLaughlin, C. Labelle, E.T. Ryan, D. Canaperi, T. Spooner, G. Bonilla, D. Edelstein, Ruthenium interconnect resistivity and reliability at 48 nm pitch, in: 2016 IEEE Int. Interconnect Technol. Conf./Adv. Met. Conf. IITC/AMC 2016, 2016, pp. 31–33, https://doi.org/10.1109/IITC-AMC.2016.7507650.

[17] S. Dutta, S. Kundu, A. Gupta, G. Jamieson, J.F.G. Granados, J. Bömmels, C. J. Wilson, Z. Tokei, C. Adelmann, Highly scaled ruthenium interconnects, IEEE Electron. Device Lett. 38 (2017) 949–951, https://doi.org/10.1109/LED.2017.2709248.

[18] L.G. Wen, C. Adelmann, O.V. Pedreira, S. Dutta, M. Popovici, B. Briggs, N. Heylen, K. Vanstreels, C.J. Wilson, S. Van Elshocht, K. Croes, J. Bommels, Z. Tokei, Ruthenium metallization for advanced interconnects, in: 2016 IEEE Int. Interconnect Technol. Conf./Adv. Met. Conf. IITC/AMC 2016, 2016, pp. 34–36, https://doi.org/10.1109/IITC-AMC.2016.7507651.

[19] L. Chen, D. Ando, Y. Sutou, J. Koike, CuAl 2 thin films as a low-resistivity interconnect material for advanced semiconductor devices, J. Vac. Sci. Technol., B 37 (2019), 031215, https://doi.org/10.1116/1.5094404.

[20] L. Chen, D. Ando, Y. Sutou, D. Gall, J. Koike, NiAl as a potential material for liner- and barrier-free interconnect in ultrasmall technology node, Appl. Phys. Lett. 113 (2018), https://doi.org/10.1063/1.5049620.

[21] C. Adelmann, L.G. Wen, A.P. Peter, Y.K. Siew, K. Croes, J. Swerts, M. Popovici, K. Sankaran, G. Pourtois, S. Van Elshocht, J. Bommels, Z. Tokei, Alternative metals for advanced interconnects, in: 2014 IEEE Int. Interconnect Technol. Conf./Adv. Met. Conf. IITC/AMC 2014, 2014, pp. 173–176, https://doi.org/10.1109/IITC.2014.6831863.

[22] L. Chen, D. Ando, Y. Sutou, M. Yahagi, J. Koike, 2020, Possibility of Cu 2 Mg for Liner-Barrier Free Interconnects, 2020, pp. 85–87.

[23] J.P. Soulie, Z. Tokei, J. Swerts, C. Adelmann, Aluminide intermetallics for advanced interconnect metallization: thin film studies, 2021, 2021, IEEE Int. Interconnect Technol. Conf. IITC (2021) 49–51, https://doi.org/10.1109/IITC51362.2021.9537441.

[24] J.P. Soulie, Z. Tokei, J. Swerts, C. Adelmann, Thickness scaling of NiAl thin films for alternative interconnect metallization, 2020, in: 2020 IEEE Int. Interconnect Technol. Conf. IITC 2020, 2020, pp. 151–153, https://doi.org/10.1109/IITC47697.2020.9515638.

[25] G.R. Caskey, J.M. Franz, D.J. Sellmyer, Electronic and magnetic states in metallic compound-II. Electron transport and magnetic susceptibility in NiAl and FeAl, J. Phys. Chem. Solid. 34 (1973) 1179–1198, https://doi.org/10.1016/S0022-3697(73)80208-2.

[26] L. Chen, D. Ando, Y. Sutou, S. Yokogawa, J. Koike, Liner- and barrier-free NiAl metallization: a perspective from TDDB reliability and interface status, Appl. Surf. Sci. 497 (2019), 143810, https://doi.org/10.1016/j.apsusc.2019.143810.

[27] D. Gall, Electron mean free path in elemental metals, J. Appl. Phys. 119 (2016), https://doi.org/10.1063/1.4942216.

[28] G. Esteves, J. Bischoff, E.W.S. Schmidt, M.A. Rodriguez, S.G. Rosenberg, P. G. Kotula, Formation of Al3Sc in Al0.8Sc0.2 thin films, Vacuum 200 (2022), https://doi.org/10.1016/j.vacuum.2022.111024.

[29] J.A. Phys, L. Chen, Y. Sutou, D. Gall, Interdiffusion Reliability and Resistivity Scaling of Intermetallic Compounds as Advanced Interconnect Materials Interdiffusion Reliability and Resistivity Scaling of Intermetallic Compounds as Advanced Interconnect Materials, 2021, 035301, https://doi.org/10.1063/5.0026837.

[30] Y. Terada, K. Ohkubo, T. Mohri, T. Suzuki, Thermal conductivity of intermetallic compounds with metallic bonding, Mater. Trans. 43 (2002) 3167–3176, https://doi.org/10.2320/matertrans.43.3167.

[31] Y. Terada, K. Ohkubo, K. Nakagawa, T. Mohri, T. Suzuki, Thermal conductivity of B2-type aluminides and titanides, Intermetallics 3 (1995) 347–355, https://doi.org/10.1016/0966-9795(95)94253-B.

[32] F. Stein, C. He, N. Dupin, Melting behaviour and homogeneity range of B2 CoAl and updated thermodynamic description of the Al-Co system, Intermetallics 39 (2013) 58–68, https://doi.org/10.1016/j.intermet.2013.03.011.

[33] T.J. Konno, S. Yamamuro, K. Sumiyama, Formation of ordered CoAl alloy clusters by the plasma-gas condensation technique, J. Appl. Phys. 90 (2001) 3079–3085, https://doi.org/10.1063/1.1394918.

[34] W. Kohn, L.J. Sham, Self-consistent equations including exchange and correlation effects, Phys. Rev. 140 (1965) A1133–A1138, https://doi.org/10.1103/PhysRev.140.A1133.

[35] P. Giannozzi, S. Baroni, N. Bonini, M. Calandra, R. Car, C. Cavazzoni, D. Ceresoli, G.L. Chiarotti, M. Cococcioni, I. Dabo, A. Dal Corso, S. De Gironcoli, S. Fabris, G. Fratesi, R. Gebauer, U. Gerstmann, C. Gougoussis, A. Kokalj, M. Lazzeri, L. Martin-Samos, N. Marzari, F. Mauri, R. Mazzarello, S. Paolini, A. Pasquarello, L. Paulatto, C. Sbraccia, S. Scandolo, G. Sclauzero, A.P. Seitsonen, A. Smogunov, P. Umari, R.M. Wentzcovitch, Quantum espresso: a modular and open-source software project for quantum simulations of materials, J. Phys. Condens. Matter 21 (2009), https://doi.org/10.1088/0953-8984/21/39/395502.

[36] N. Troullier, J.L. Martins, Title No, Phys. Rev. B 43 (1991) 1993.

[37] M. Schlipf, F. Gygi, Optimization algorithm for the generation of ONCV pseudopotentials, Comput. Phys. Commun. 196 (2015) 36–44, https://doi.org/10.1016/j.cpc.2015.05.011.

[38] J.P. Perdew, Y. Wang, Erratum: accurate and simple analytic representation of the electron-gas correlation energy, 13244, Phys. Rev. B (1992) 45, https://doi.org/10.1103/PhysRevB.98.079904, 10.1103/PhysRevB.45.13244), Phys. Rev. B. 98 (2018) 244–249.

[39] D.R. Hamann, Optimized norm-conserving Vanderbilt pseudopotentials, Phys. Rev. B Condens. Matter 88 (2013) 1–10, https://doi.org/10.1103/PhysRevB.88.085117.

[40] S. Baroni, S. de Gironcoli, A. Dal Corso, P. Giannozzi, Phonons and related crystal properties from density-functional perturbation theory, Rev. Mod. Phys. 73 (2001) 515–562, https://doi.org/10.1103/RevModPhys.73.515.

[41] S. Poncé, E.R. Margine, C. Verdi, F. Giustino, EPW: electron–phonon coupling, transport and superconducting properties using maximally localized Wannier functions, Comput. Phys. Commun. 209 (2016) 116–133, https://doi.org/10.1016/j.cpc.2016.07.028.

[42] S. Poncé, E.R. Margine, F. Giustino, Towards predictive many-body calculations of phonon-limited carrier mobilities in semiconductors, Phys. Rev. B 97 (2018) 1–5, https://doi.org/10.1103/PhysRevB.97.121201.

[43] N. Marzari, A.A. Mostofi, J.R. Yates, I. Souza, D. Vanderbilt, Maximally localized Wannier functions: theory and applications, Rev. Mod. Phys. 84 (2012) 1419–1475, https://doi.org/10.1103/RevModPhys.84.1419.

[44] I. Souza, N. Marzari, D. Vanderbilt, Maximally localized Wannier functions for entangled energy bands, Phys. Rev. B Condens. Matter 65 (2002) 1–13, https://doi.org/10.1103/PhysRevB.65.035109.

[45] N. Marzari, D. Vanderbilt, Maximally localized generalized Wannier functions for composite energy bands, Phys. Rev. B Condens. Matter 56 (1997) 12847–12865, https://doi.org/10.1103/PhysRevB.56.12847.

[46] J. Noffsinger, F. Giustino, B.D. Malone, C.H. Park, S.G. Louie, M.L. Cohen, EPW, A program for calculating the electron-phonon coupling using maximally localized Wannier functions, Comput. Phys. Commun. 181 (2010) 2140–2148, https://doi.org/10.1016/j.cpc.2010.08.027.

[47] G.K.H. Madsen, D.J. Singh, BoltzTraP. A code for calculating band-structure dependent quantities, Comput. Phys. Commun. 175 (2006) 67–71, https://doi.org/10.1016/j.cpc.2006.03.007.

[48] L.M. Pike, Y.A. Chang, C.T. Liu, Point defect concentrations and hardening in binary B2 intermetallics, Acta Mater. 45 (1997) 3709–3719, https://doi.org/10.1016/S1359-6454(97)00028-1.

[49] S.N. Hosseini, T. Mousavi, F. Karimzadeh, M.H. Enayati, Thermodynamic aspects of nanostructured CoAl intermetallic compound during mechanical alloying, J. Mater. Sci. Technol. 27 (2011) 601–606, https://doi.org/10.1016/S1005-0302(11)60114-X.

[50] S. Mahieu, P. Ghekiere, D. Depla, R. De Gryse, Biaxial alignment in sputter deposited thin films, Thin Solid Films 515 (2006) 1229–1249, https://doi.org/10.1016/j.tsf.2006.06.027.

[51] D.H. Choi, Y.D. Han, B.K. Lee, S.J. Choi, H.C. Yoon, D.S. Lee, J.B. Yoon, Use of a columnar metal thin film as a nanosieve with sub-10 nm pores, Adv. Mater. 24 (2012) 4408–4413, https://doi.org/10.1002/adma.201200755.

[52] W.W.Y. Lee, High resistivity of dc-sputtered metal films, J. Appl. Phys. 42 (1971) 4366–4370, https://doi.org/10.1063/1.1659781.

[53] P. Khwansungnoen, T. Chaiyakun, S. Suwanboon, T. Rattana, The influence of nitrogen partial pressure on visible-light-driven photocatalytic activity of sputtered titanium oxynitride thin films, Vacuum 193 (2021), 110540, https://doi.org/10.1016/j.vacuum.2021.110540.

[54] M. Zubkins, I. Aulika, E. Strods, V. Vibornijs, L. Bikse, A. Sarakovskis, G. Chikvaidze, J. Gabrusenoks, H. Arslan, J. Purans, Optical properties of oxygen-containing yttrium hydride thin films during and after the deposition, Vacuum 203 (2022), 111218, https://doi.org/10.1016/j.vacuum.2022.111218.

[55] Y. Yamaguchi, D.A. Kiewit, T. Aoki, J.O. Brittain, Electrical resistivity of NiAl, CoAl, NiGa, and CoGa, J. Appl. Phys. 39 (1968) 231–232, https://doi.org/10.1063/1.1655738.

[56] P.M. Echenique, J.M. Pitarke, E.V. Chulkov, A. Rubio, Theory of inelastic lifetimes of low-energy electrons in metals, Chem. Phys. 251 (2000) 1–35, https://doi.org/10.1016/S0301-0104(99)00313-4.

[57] V.A. Marsocci, S.S. Shue, Influence of the specularity coefficient of surface scattering in the Leonard-Ramey relations for metallic thin films, J. Appl. Phys. 42 (1971) 5047–5050, https://doi.org/10.1063/1.1659889.

[58] Z. Tong, S. Li, X. Ruan, H. Bao, Comprehensive first-principles analysis of phonon thermal conductivity and electron-phonon coupling in different metals, Phys. Rev. B 100 (2019), https://doi.org/10.1103/PhysRevB.100.144306.

[59] D.B. Miracle, Overview No. 104 the physical and mechanical properties of NiAl, Acta Metall. Mater. 41 (1993) 649–684, https://doi.org/10.1016/0956-7151(93)90001-9.

[60] Z. Tong, S. Li, X. Ruan, H. Bao, Comprehensive first-principles analysis of phonon thermal conductivity and electron-phonon coupling in different metals, Phys. Rev. B 100 (2019), 144306, https://doi.org/10.1103/PhysRevB.100.144306.

[61] P. Review, I. Apart, E. The, Low-Temperature Resist. 25 (1982) 3865–3870.

[62] J.L. Murray, The Aluminium-Copper, 1985, p. 30.

[63] A.H. Johnstone, CRC handbook of chemistry and physics-69th edition, 1988, pp. 2400, price £57.50, in: R.C. Chief, Weast (Eds.), Boca Raton, Florida, vol. 50CRC Press Inc., 2007, pp. 294–295, https://doi.org/10.1002/jctb.280500215. ISBN 0-8493-0369-5 J. Chem. Technol. Biotechnol.

[64] B.A. Sanborn, P.B. Allen, D.A. Papaconstantopoulos, Empirical electron-phonon coupling constants and anisotropic electrical resistivity in hcp metals, Phys. Rev. B 40 (1989) 6037–6044, https://doi.org/10.1103/PhysRevB.40.6037.

[65] H. Bishara, M. Ghidelli, G. Dehm, Approaches to measure the resistivity of grain boundaries in metals with high sensitivity and spatial resolution: a case study employing Cu, ACS Appl. Electron. Mater. 2 (2020) 2049–2056, https://doi.org/10.1021/acsaelm.0c00311.

[66] J. Koike, T. Kuge, L. Chen, M. Yahagi, Intermetallic compounds for interconnect metal beyond 3 nm node, 2021, 2021, IEEE Int. Interconnect Technol. Conf. IITC (2021) 34–36, https://doi.org/10.1109/IITC51362.2021.9537364.